Check for updates

Advanced theoretical design of light-driven molecular rotary motors: enhancing thermal helix inversion and visible-light activation†

Weiliang Shi,[a] Jianzheng Ma,[b] Chenwei Jiang (iD) *[b] and Tetsuya Taketsugu (iD) *[cd]

In this study, we have advanced the field of light-driven molecular rotary motors (LDMRMs) by achieving two pivotal goals: lowering the thermal helix inversion (THI) barrier and extending the absorption wavelength into the visible spectrum. This study involves the structural reengineering of a second-generation visible LDMRM, resulting in the synthesis of a novel class, specifically, 2-((2S)-5-methoxy-2-methyl-2,3-dihydro-1H-cyclopenta[a]naphthalen-1-yl)-3-oxo-2,3-dihydro-1H-dibenzo[e,g]indole-6,9-dicarbonitrile. This redesigned motor stands out with its two photoisomerization stages and two thermal helix inversions, featuring exceptionally low THI barriers (4.00 and 2.05 kcal mol^{-1} at the OM2/MRCI level for the EM → EP and ZM → ZP processes, respectively). Moreover, it displays absorption wavelengths in the visible light range (482.98 and 465.76 nm for the EP and ZP isomers, respectively, at the TD-PBE0-D3/6-31G(d,p) level), surpassing its predecessors in efficiency, as indicated by the narrow HOMO−LUMO energy gap. Ultrafast photoisomerization kinetics (approximately 0.8–1.6 ps) and high quantum yields (around 0.3−0.6) were observed through trajectory surface hopping simulations. Additionally, the simulated time-resolved fluorescence emission spectrum indicates a significantly reduced "dark state" duration (0.09–0.26 ps) in these newly designed LDMRMs compared to the original ones, marking a substantial leap forward in the design and efficiency of LDMRMs.

1. Introduction

Molecular motors[1–3] have the remarkable ability to induce mechanical rotation through precise movements of their constituent components, triggered by electronic or chemical stimuli, particularly the influence of light. The prospect of harnessing light as a potent energy source for molecular motors has garnered growing interest in recent years. This interest stems from the unique advantages of light-driven molecular motors (LDMRMs), where specific wavelengths of light can control their operation without the need for physical contact or dependence on the surrounding environment, all while minimizing the generation of waste byproducts.[4,5] LDMRMs operate through the photoisomerization of the alkene framework, with the two molecular motor subcomponents connected by a double C=C or C=N bond, enabling them to absorb activating light and achieve a full 360° rotation.[4–7]

Most LDMRMs traditionally rely on ultraviolet (UV, 100–400 nm) or visible (400–750 nm) light for their excitation. This approach comes with several drawbacks: UV light is undesirable for constructing nodular photoresponsivity systems;[3] UV light is less than ideal for constructing compact photoresponsive systems, and it can be detrimental to materials prone to degradation, while also posing a risk to cell health due to photoreactions in some cellular components.[8] Consequently, shifting the absorption band of the chromophore to the visible or near-infrared region of the electromagnetic spectrum has become a central concern within the LDMRM field. Various strategies have been explored to achieve a redshift of the excitation wavelength for well-established LDMRMs. Among these approaches, the most effective is believed to be the fine-tuning of the highest occupied molecular orbital (HOMO)–lowest unoccupied molecular orbital (LUMO) band gap through structural modifications of the molecular motor. In 2003, the Feringa group introduced a groundbreaking concept by proposing a donor–acceptor functionalized LDMRM,

[a] Graduate School of Chemical Sciences and Engineering, Hokkaido University, Sapporo 060-0810, Japan

[b] Ministry of Education Key Laboratory for Nonequilibrium Synthesis and Modulation of Condensed Matter, Shaanxi Province Key Laboratory of Quantum Information and Quantum Optoelectronic Devices, School of Physics, Xi'an Jiaotong University, Xi'an 710049, China. E-mail: jiangcw@xjtu.edu.cn

[c] Department of Chemistry, Faculty of Science, Hokkaido University, Sapporo 060-0810, Japan. E-mail: take@sci.hokudai.ac.jp

[d] Institute for Chemical Reaction Design and Discovery (WPI-ICReDD), Hokkaido University, Sapporo 001-0021, Japan

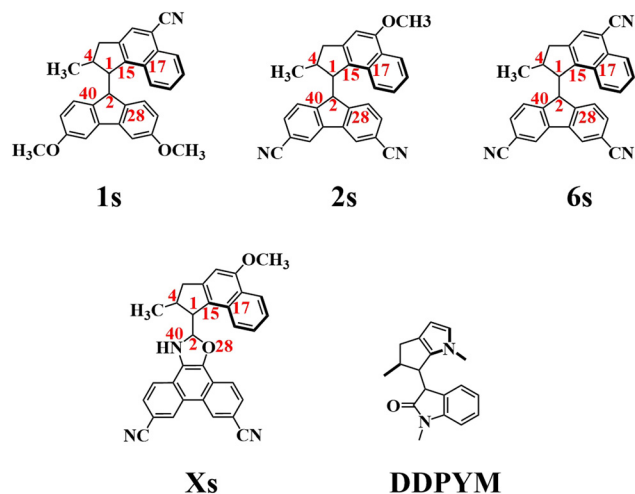† Electronic supplementary information (ESI) available. See DOI: https://doi.org/10.1039/d4cp00037d

15672 | *Phys. Chem. Chem. Phys.*, 2024, **26**, 15672–15680

This journal is © the Owner Societies 2024

Fig. 1 The geometry of rotary motor 1s, 2s, 6s, and the newly designed Xs, as well as DDPYM. Some atoms are labelled by red numbers.

enabling the absorption of photons at 430 nm through the introduction of a push–pull system in the lower half of the molecular motor, facilitating photoisomerization.[9] More recently, Leeuwen and colleagues[10] introduced a class of LDMRMs based on the push–pull system. The incorporation of a benzofluorenyl moiety into a standard molecular motor resulted in a considerable bathochromic shift, with λ_{max} transitioning from 395 nm of the parent motor to 420 nm due to enhanced π-conjugation. Pfeifer et al.[11] further delved into the structural redesign of the second-generation LDMRM based on a push–pull system, achieving an even more pronounced redshift in the maximum absorption wavelength by altering substituents in the stator and rotor. In their study, three push–pull motors and a tricyano-substituted motor (1s, 2s, 6s refer to Fig. 1) were prepared, allowing for a comparative analysis of the impact of push–pull substitution on π-system extension by the CN-group in 6s.[11] The results revealed maximum absorption wavelengths of 422 nm (1s), 453 nm (2s), and 421 nm (6s), with quantum yields ranging from approximately 0.3–0.11. These findings underscore the potential for achieving a redshift in absorption wavelength through strategic structural design, such as the introduction of substituent groups.[12,13]

Feringa-type molecular motors exist in two main configurations: 4-stroke (involving two steps of photoisomerization coupled with two steps of thermal helix inversion (THI)),[12,13] and 2-stroke (consisting of two photoisomerization steps only).[14] The timescales for the photoisomerization and THI steps span from nanoseconds to days and femtoseconds to picoseconds, respectively.[15,16] The rotation speed of a designed LDMRM is influenced by all the constituent steps in its rotation cycle, and the high energy barrier associated with the THI step hinders the overall rotation speed of LDMRMs. Hence, there exists considerable potential for enhancing the rotation speed by reducing the THI barrier.[3] Recently, a new family of fulgide-based LDMRMS was reported by Filatov et al.[17] They investigated the dynamics properties of these prototype molecules using a combination of quantum chemical calculations and

trajectory surface hopping (TSH) simulations with Tully's fewest switches algorithm.[18] The TSH method is a highly effective technique for exploring the elementary processes of excited-state dynamics by calculating potential gradients through electronic structure calculations to determine the forces acting on atoms, deriving classical trajectories through numerical solutions of Newton's equations of motion, and considering transitions between electronic states due to non-adiabatic couplings.[19,20] Theoretical simulations predicted a quantum efficiency of 0.55–0.68 for these prototype molecules, an ultrafast dynamics timescale of 200 to 300 fs, and a thermal helix potential barrier of 13.6 kcal mol^{-1}.

Several new designs of LDMRMs have been theoretically proposed to augment the rotation speed by minimizing the THI step. Filatov et al.[21] reported a new class of 2-stroke LDMRM capable of 360° rotation by reengineering the rotor blades and combining two photoisomerization steps. The TSH simulations predicted a photoisomerization process taking place within a timescale of 200 to 300 fs, demonstrating a notably high quantum yield of approximately 0.91–0.97. García-Iriepa et al.[22] proposed a 2-stroke photoreaction-only LDMRM that eliminates the THI step and achieves rapid rotation by introducing a chiral hydrogen bond environment. More recently, Ma et al.[23] introduced a new 3-stroke LDMRM capable of a full 360° rotation in two photoisomerization steps and one THI step, named DDIYs. TSH simulations at the semi-empirical OM2/MRCI level predicted ultrafast timescales (0.1 to 0.3 fs) for the two photoisomerization steps. They also designed an oxindole-based LDMRM, DDPYM,[24] with a push–pull character and minimal steric hindrance near the rotation axis, leading to faster and more concentrated electronic decay of the S$_1$ excited state compared to its parent molecule.

Consequently, significant research endeavors have been dedicated to shifting the absorption wavelength of molecular motors into the visible spectrum while upholding rotation speed and quantum yield. Drawing inspiration from the oxindole-based LDMRM, we introduce a new category of 4-stroke light-driven molecular motors, denoted as 2-((2S)-5-methoxy-2-methyl-2,3-dihydro-1H-cyclopenta[a]naphthalen-1-yl)-3-oxo-2,3-dihydro-1H-dibenzo[e,g]indole-6,9-dicarbonitrile, or simply "Xs" (Fig. 1). Our molecule design draws from the second-generation LDMRMs established by Pfeifer et al.,[11] focusing on tuning the HOMO–LUMO energy gap and minimizing the THI barrier. This adaptation enables a 360° rotation that encompasses two-step photoisomerization (EP to ZM and ZP to EM) and two-step thermal helix inversion. The primary aim was to conduct a comprehensive assessment of key attributes, including the UV-visible (UV-vis) spectrum, time-resolved fluorescence emission spectrum, the THI barrier, quantum yield, and average lifetime. These comparative analyses allowed us to evaluate and validate the performance of the designed LDMRM. Furthermore, we conducted a detailed comparative analysis with a recently conceived oxindole-based LDMRM named "DDPYM" (Fig. 1). We believe that this innovatively designed LDMRM will serve as a catalyst for further experimental and theoretical research in this domain.

This journal is © the Owner Societies 2024

Phys. Chem. Chem. Phys., 2024, **26**, 15672–15680 | **15673**

2. Computational details

The equilibrium and transition state structures of LDMRMs 1s, 2s, 6s, and Xs in the ground state were optimized, and normal mode analyses were conducted through DFT calculations employing B3LYP-D3, CAMB3LYP-D3, M06-2X, and ωB97XD functionals along with 6-31G(d,p) basis sets. Additionally, the geometry optimization for isomers EP and ZP was carried out at the PBE0-D3/6-31G(d,p) level. UV-vis absorption spectra were calculated using TDDFT at the same computational level. All DFT and TDDFT calculations were executed using the Gaussian09 program.[25]

The OM2/MRCI method, recognized for its computational efficiency and accuracy in exploring excited state dynamics, has been widely used in the investigation of photochemical reactions,[26–37] as evident in benchmark papers.[38–42] In this study, the OM2/MRCI method, implemented in the MNDO99 program,[43] was utilized for excited-state calculations and dynamics simulations of LDMRMs 1s, 2s, 6s, and Xs. The Lagrange–Newton approach[44] facilitated the identification of S_1/S_0 minimum energy conical intersections (MECIs) along the photoisomerization pathways. Multireference configuration interaction (MRCI) calculations were conducted for three reference states, encompassing the closed-shell ground-state, and single and double excitations from HOMO to LUMO. Considering the characteristics of $\pi\pi^*$ electronic excitations and the convergence of the optimizations for MECIs, we selected active spaces (8,9), (10,10), (8,8), and (8,8) for the three substituent molecular motors, 1s, 2s, 6s, and Xs, respectively, in the OM2/MRCI calculations. To ensure the persistence of π orbitals within the active space throughout the calculation process, we identified and tracked the π-type population (PIPOP) using a threshold of 0.4.

The TSH simulations were conducted for molecular motors within the framework of the OM2/MRCI method utilizing Tully's fewest-switches algorithm.[18] Initial conditions were generated by the ground state equilibrium structure, with atomic velocities randomly distributed according to a Wigner distribution at 300 K. Geometries were selectively chosen using the filtering approach integrated into the MNDO program.[43] In this filtering approach, transition probabilities are calculated for structures generated via Wigner sampling, and structures are then selected as initial conditions based on a comparison between these transition probabilities and random numbers.[45] Wigner sampling is based on harmonic normal modes, and when it includes low-frequency modes, it samples structures that deviate from the equilibrium configuration. This can be problematic because in the actual potential energy surfaces of molecular systems, the effects of anharmonicity and mode coupling contribute, which reduces the accuracy of structural sampling along low-frequency modes. A simple workaround is to exclude these low-frequency modes from the sampling. However, more precise methods such as the quantum thermostat technique have been devised recently, and comparisons between these methods and experimental data are being made.[46] Although the molecular system in the current study includes low-frequency modes, the purpose of the TSH simulations using OM2/MRCI is qualitative rather than quanti-

tative, so we used conventional Wigner sampling to set the initial conditions. To enhance accuracy, the empirical decoherence correction proposed by Granucci et al.[47] (0.1 a.u.) was applied. The Newton equation of motion was resolved employing a time step of 0.1 fs through the velocity-Verlet algorithm,[48] while the time-dependent electronic Schrödinger equation was solved with a time step 100 times smaller.

3. Results and discussion

3.1. Structures and potential energy profiles for molecular motor

Concerning the geometries of 1s, 2s, 6s, and Xs, we adopt the helicity definition proposed by Karnik et al.[49] According to conformation and helicity, two equilibrium geometries of different parent molecules, 1s, 2s, and 6s, are denoted as P and M, while four equilibrium geometries of Xs are labeled EP, ZM, ZP, and EM. Fig. 1 depicts the most stable geometries for 1s (P) and Xs (EP), respectively. Fig. S1, S3, S5 and S6 (refer to ESI†) present all geometries of 1s, 2s, 6s, and Xs, with corresponding structural parameters calculated at different levels outlined in Tables S1, S4, S7 and S10 (refer to ESI†). It is evident that results from various calculation levels are in agreement with each other. The dihedral angles $C_{40}–C_2–C_1–C_{15}$ and $C_2–C_1–C_{15}–C_{17}$ are employed to characterize the steric bulkiness in the fjord region for 1s-P, 2s-P, 6s-P, Xs-EP, and Xs-ZP. Tables S1, S4, S7, and S10 (ESI†) indicate that the dihedral angles for 1s-P, 2s-P, 6s-P are all smaller than those for Xs-EP and Xs-ZP, suggesting that the steric bulkiness in the fjord region is less pronounced for Xs-EP and Xs-ZP compared to 1s-P, 2s-P and 6s-P.

Fig. 2 and 3 illustrate schematic diagrams of potential energy profiles for the rotation cycle of the molecular motors 1s and Xs, respectively. Table 1 presents the calculated energy barriers for 1s, 2s, 6s (between M and P), and Xs (between ZM and ZP and between EM and EP) in the ground state, calculated using the OM2/MRCI method. The optimized transition state geometries are depicted in Fig. S1, S3, S5 and S6 (ESI†), and corresponding structural parameters are provided in Tables S1, S4, S7 and S10 (ESI†). The OM2/MRCI results align well with those obtained through DFT calculations. As depicted in Fig. 2 and 3, the molecular motor undergoes photoexcitation to the FC region (P isomer for 1s and EP and ZP isomers for Xs). Subsequently, the molecular motor rotates counterclockwise around the C=C double bond, decaying to the ground state via S_1/S_0 CIs, and eventually reaching stable M isomers for 1s and ZM or EM isomers for Xs. Over time, the stable M isomers of 1s and ZM or EM isomers of Xs traverse the THI barrier and isomerize to P′ of 1s and ZP of EP isomers for Xs. Table 1 reveals that the relative values of THI barriers for 1s, 2s, 6s, and Xs are consistent regardless of the method used. The THI barriers of the newly designed molecular motor Xs are notably lower than those of 1s, 2s, and 6s, suggesting a potentially higher rotational speed for Xs compared to 1s, 2s, and 6s. In comparison to DDPYM, the THI barriers of Xs are higher than DDPYM between ZM and ZP, while THI barriers between
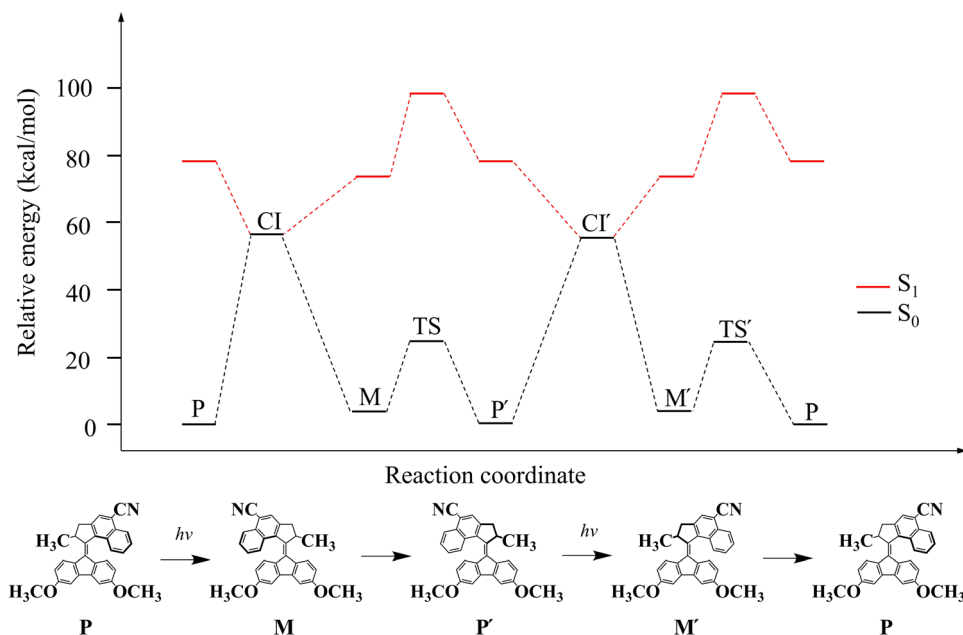
15674 | Phys. Chem. Chem. Phys., 2024, 26, 15672–15680

This journal is © the Owner Societies 2024

Fig. 2 The energy profiles of S_0 and S_1 states of a rotation cycle for the molecular motor 1s (P → M → P′ → M′ → P) at the OM2/MRCI level; CI and TS denote conical intersection and transition state, respectively.
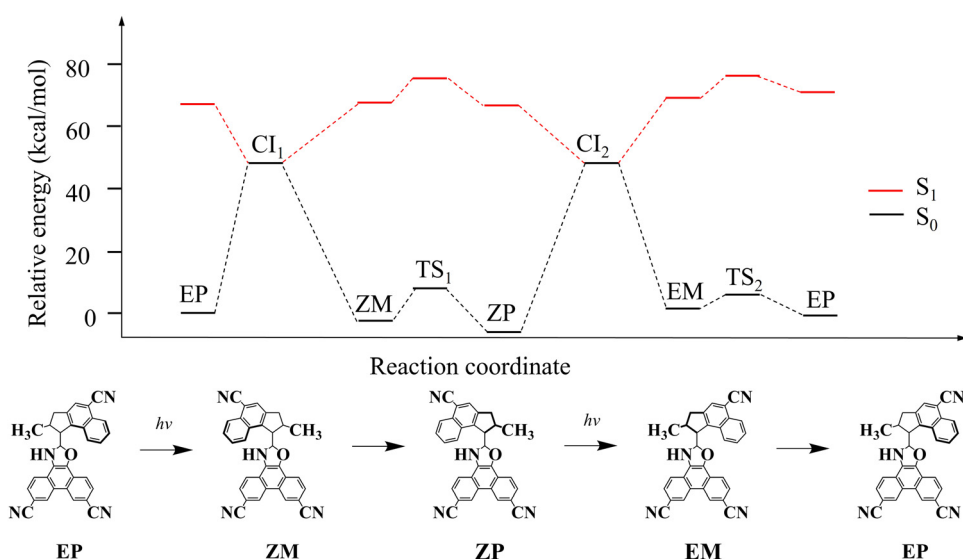
Fig. 3 The energy profiles of S_0 and S_1 states of a rotation cycle for the molecular motor Xs (EP → ZM → ZP → EM → EP) at the OM2/MRCI level; CI and TS denote conical intersection and transition state, respectively.

EM and EP are lower. This implies that the rotational speed of Xs may differ from DDPYM depending on the specific isomerization pathway, with Xs being faster for EM to EP and potentially slower for ZM to ZP. Fig. S2 and S4 (refer to ESI†) provide a similar schematic diagram of potential energy profiles for 2s and 6s.

3.2. Absorption spectrum

To evaluate the performance of the newly designed Xs molecular motor, we conducted calculations of Ultraviolet-visible

(UV-vis) absorption spectra using the TDDFT method. These calculations were carried out for the optimized structures of 1s, 2s, 6s, Xs, and DDPYM at the PBE0-D3 level. The $S_0 \rightarrow S_1$ excitation energy was homogeneously broadened with a full width at half maximum (FWHM) of 0.5 eV using Gaussian function expansion. The absorption wavelengths (in nm) and excitation energies (in eV) for the S_1 state calculated by TDDFT and OM2/MRCI are shown in Table 2, and the corresponding absorption spectra derived from the excited states of S_1–S_6 are depicted in Fig. 4(a); the corresponding experimental absorption

Table 1 The THI barriers for 1s, 2s, 6s, and Xs at the levels of OM2/MRCI, B3LYP-D3, CAMB3LYP-D3, M06-2X, and wB97XD. The energy is given in kcal mol^{-1}

		OM2/MRCI	B3LYP-D3	CAMB3LYP-D3	M062X	ωB97XD
1s	M → P′	19.80	22.06	21.52	21.80	21.52
2s	M → P′	20.59	23.50	22.95	23.13	22.92
6s	M → P′	20.01	22.95	22.51	22.75	22.46
Xs	ZM → ZP	4.00	5.74	5.33	4.66	4.87
	EM → EP	2.05	6.26	6.35	7.17	6.47
DDPYM[24]	ZM → ZP	2.00	—	—	—	—
	EM → EP	8.80	—	—	—	—

spectra for 1s, 2s, and 6s[11] are also presented in Fig. 4(b) for comparison. In Fig. 4(a), molecular motors 1s, 2s, 6s, and Xs exhibit absorption peaks ranging from 350 to 600 nm. The maximum absorption wavelengths for motors 1s, 2s, and 6s, calculated using TDDFT, are 445.28, 422.21, and 425.22 nm, respectively. These values align well with the corresponding experimental data, even though the maximum absorption wavelengths for 1s and 2s have been reversed. We have also performed TDDFT calculations considering solvent effects on the excitation energy of the S_1 state, and compared these results with those obtained in the gas phase (see Table S13 in the ESI†). Conversely, the newly designed motor Xs shows maximum absorption wavelengths (EP and ZP) at 482.98 nm and 465.76 nm, respectively. Notably, these values represent a significant redshift when compared to the absorption wavelengths of 1s, 2s, and 6s. Furthermore, in comparison to the EP and ZP values of DDPYM, motor Xs exhibits a substantial redshift of 89.98 nm and 129.76 nm, respectively.

The overall UV-vis spectra generated from Wigner sampling and absorption spectra at the OM2/MRCI level were also calculated and are shown in Fig. S7(a) and (b) (ESI†), respectively, with maximum absorption wavelengths listed in Table 2. The absorption spectra of 1s, 2s, 6s, and Xs span from 250 to 550 nm, qualitatively alligning with TDDFT calculations. Notably, the maximum absorption wavelength of Xs (EP and ZP) is greater than that observed for 1s, 2s, and 6s, which can also be shown in Fig. S7(b) (ESI†). The consistency between the several sets of results indicates that the newly designed motors exhibit a significant redshift in the UV-vis absorption spectrum. To further elucidate the reason for the redshift of Xs, we examined the relevant frontier molecular orbitals. As illustrated in Fig. 5,

the HOMO–LUMO energy gap of molecular motor Xs is notably low compared to the substituent motors 1s, 2s, and 6s. The structural modification of Xs has reduced the HOMO–LUMO energy gap by altering the HOMO and LUMO charge distribution. Consequently, the maximum wavelengths of the UV-vis absorption spectra of the newly designed molecular motor Xs were red-shifted to 482.98 and 465.76 nm.

3.3. Trajectory surface hopping simulations

Trajectory surface hopping (TSH) simulations were systematically conducted to explore the photoisomerization processes of 1s, 2s, 6s, and Xs. Initially, for each system, the CI of S_1/S_0 was optimized at the OM2/MRCI level. The relevant geometric structure data are summarized in Tables S2, S5, S8 and S11 (ESI†). Fig. S1, S3, and S5 (ESI†) illustrate that the obtained S_1/S_0 CI points for 1s, 2s, and 6s are distinguished by different dihedral angles $\theta_{4-1-2-28}$ and $\theta_{15-1-2-28}$. For Xs, the four S_1/S_0 CI points, denoted as CI_1 and CI_2, are identified based on the dihedral angles $\theta_{4-1-2-28}$ and $\theta_{15-1-2-28}$ (refer to Fig. 1 for key atomic labels), as shown in Fig. S6 (refer to ESI†). The CI geometries obtained for 1s, 2s, 6s, and Xs all exhibit pronounced pyramidalization at the carbon atoms of the stator-axle, a phenomenon reported in other molecular motor studies.[3,23,27,50,51] To directly observe the pyramidalization phenomenon during dynamics simulations, the time dependence of the dihedral angles $\theta_{4-1-2-28}$, $\theta_{15-1-2-28}$, $\theta_{2-40-28-1}$ for 1s, 2s, 6s, and Xs in one representative trajectory is presented in Fig. S8(a), S9(a), S10(a), and S11(a) (refer to ESI†). As the trajectories approach the CI region, the dihedral angle $\theta_{2-40-28-1}$ (1s, 2s, 6s) reaches about 30°, and the dihedral angle $\theta_{2-40-28-1}$ (Xs-EP, Xs-ZP) also gradually increase to about 20°. This observation indicates that the pyramidalization of carbon atoms at the stator-axle becomes evident in the dynamics simulations.

For 1s, 2s, 6s, Xs (EP), and Xs (ZP), 400 structures were generated, respectively, using Wigner sampling. Through the filtering approach, about 70% of these structures were selected. From the chosen structures, 175, 242, 233, 220, and 179 structures, respectively, were selected as initial conditions for trajectory calculations, and we conducted TSH simulations from the S_1 excited state. The simulation times were 5.0, 2.5, 5.0, 1.5, and 3.0 ps for each molecular species. Isomerization to M was achieved for 1s, 2s, and 6s by counterclockwise rotation around the central C=C double bond, with quantum yields of approximately 0.78, 0.6, and 0.67, respectively. For Xs, the photoisomerization process was investigated for EP and ZP

Table 2 The absorption wavelengths (in nm) and excitation energies (in eV) for the S_1 state of the molecules 1s, 2s, 6s, Xs, and DDPYM, calculated using two methods: TDDFT with PBE0-D3/6-31G(d,p) and OM2/MRCI. The experimental data for 1s-P, 2s-P, and 6s-P measured in dichloromethane (DCM) solvent[11] are also presented

		TDDFT	OM2/MRCI	Exp.
1s	P	445.28/2.78	364.5/3.40	422/2.94
2s	P	422.21/2.94	362.5/3.42	453/2.74
6s	P	425.22/2.92	353.0/3.51	421/2.95
Xs	EP	482.98/2.57	395.0/3.14	
	ZP	465.76/2.66	382.5/3.24	
DDPYM	EP	385.99/3.21		
	ZP	383.00/3.23		

15676 | Phys. Chem. Chem. Phys., 2024, 26, 15672–15680

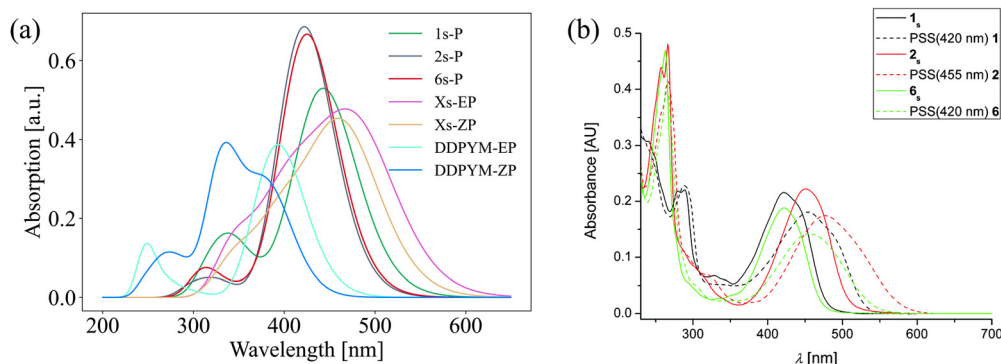This journal is © the Owner Societies 2024

Fig. 4 (a) UV-Vis spectra and equilibrium structures of 1s, 2s, 6s, Xs, and DDPYM determined in the gas phase by TDDFT calculations at the PBE0-D3/6-31G(d,p) level. (b) The experimental spectra for 1s, 2s, and 6s (Solid lines: UV-vis spectra of 1s, 2s, and 6s in dichloromethane solvent. Dashed lines: UV-vis spectra after irradiation to photo-stationary states (PSS) with 420 nm (1s, 6s) and 455 nm (2s) light) (Reproduced from ref. 11 with permission from the Royal Society of Chemistry).
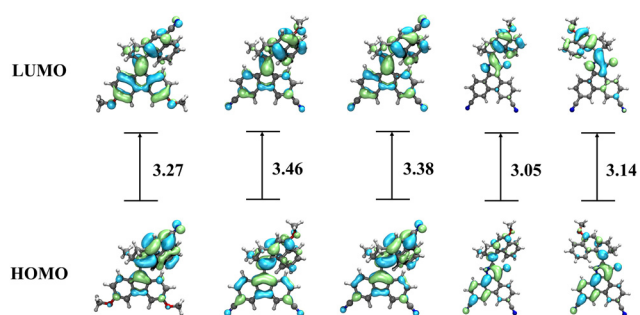

Fig. 5 The HOMO and LUMO of motor 1s-P, 2s-P, 6s-P, Xs-EP, and Xs-ZP, calculated at the PBE0-D3/6-31G(d,p) level, with HOMO–LUMO gap in eV.

starting from the S_1 excited state, with quantum yields of approximately 0.55 and 0.37 for EP $\rightarrow$ ZM and ZP $\rightarrow$ EM,

respectively. In the case of DDPYM, the quantum yield for the transition from EP to ZM is 0.52, and for the transition from ZP to EM is 0.36. Which is comparable to Xs. Fig. 6 illustrates the time evolution of the S_0 and S_1 state populations for 1s, 2s, 6s, Xs-EP, and Xs-ZP. The average lifetimes of the S_1 state for each molecular species are calculated to be 2.56, 1.16, 2.40, 0.85, and 1.85 ps, respectively. Table 3 presents the number of trajectories, quantum yields, and lifetimes. The newly designed molecular motor Xs exhibits a slight decrease in the quantum yield of the photoisomerization reaction compared to 1s, 2s, and 6s. The time evolution of the population reveals that the average lifetime of the EP $\rightarrow$ ZM isomerization of Xs is extremely short compared to 1s, 2s, and 6s, and the ZP $\rightarrow$ EM isomerization reaction is also significantly shorter than that of 1s and 6s. Indeed, when comparing the simulated average lifetimes of DDPYM for the EP $\rightarrow$ ZM (0.27) and
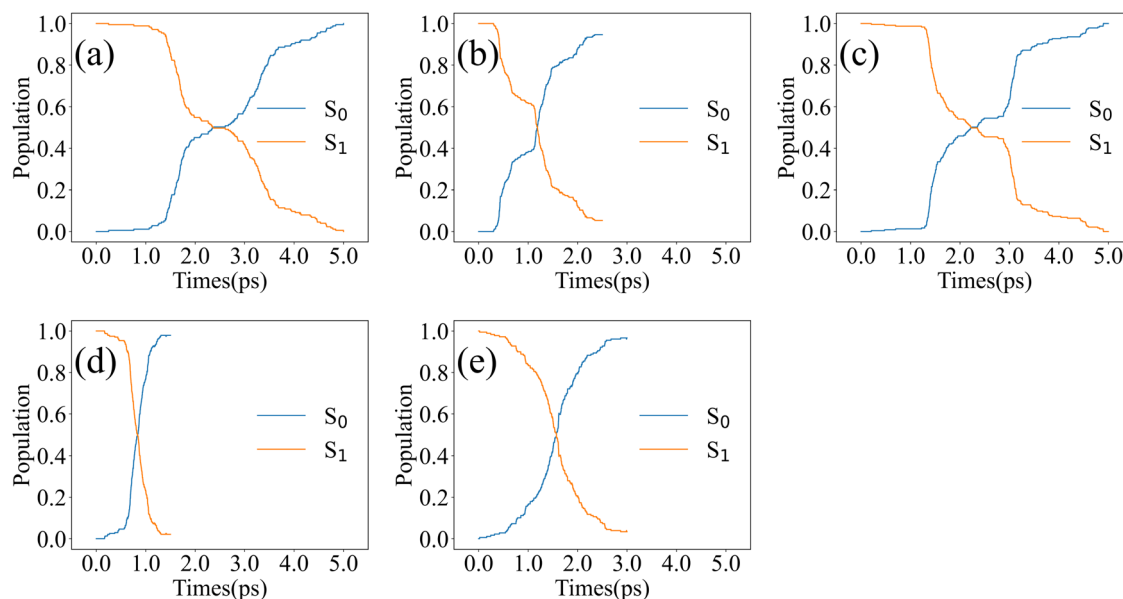

Fig. 6 The average population of electronic states S_0 and S_1 over simulation time in the photoisomerization process starting from (a) 1s-P, (b) 2s-P, (c) 6s-P, (d) Xs-EP, and (e) Xs-ZP isomers.
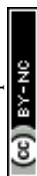
This journal is © the Owner Societies 2024

Phys. Chem. Chem. Phys., 2024, **26**, 15672–15680 | **15677**

Table 3 The simulated quantum yields and average lifetimes for the photoisomerization of 1s, 2s, 6s, and Xs

		Number of trajectories	Quantum yields	Average lifetime (ps)
1s	P–M	175	0.78	2.56
2s	P–M	242	0.60	1.16
6s	P–M	233	0.67	2.40
Xs	EP–ZM	220	0.55	0.85
	ZP–EM	179	0.37	1.58
DDPYM[24]	EP–ZM	238	0.52	0.27
	ZP–EM	221	0.36	0.44

ZP → EM (0.44), it becomes evident that the lifetimes in DDPYM are significantly shorter than those in Xs. This suggests that Xs may exhibit longer-lived excited states compared to DDPYM.

To provide further insight into the reduced lifetime of Xs-EP and Xs-ZP compared to 1s, 2s, and 6s, we conducted nonadiabatic dynamics simulations of the photoisomerization process to compute the "dark state" duration. The dark state duration was determined based on the obtained average lifetime and the time-dependent fluorescence emission spectrum presented in Fig. S12a, S13a, S14a, S15a, and S16a (ESI†), with the corresponding data listed in Table S15 (ESI†). It is important to note that the term "dark state" in this context does not refer to a new electronic state but rather signifies a "dark region" with low oscillator strength on the excited state.[27] The computational details of the time-dependent fluorescence emission spectrum and a more comprehensive description of the computational results can be found in the ESI.† As indicated in Table S15 (ESI†), the "dark state" durations for 1s, 2s, and 6s are 1.86, 0.90, and 2.06 ps, respectively, which are significantly longer than those for Xs-EP and Xs-ZP at 0.09 and 0.26 ps. This observation may elucidate why the average lifetime of the EP → ZM process for XS is extremely shorter than that for 1s, 2s, and 6s, and the ZP → EM process is also significantly shorter than that for 1s and 6s. The slightly higher average lifetime of ZP → EM process for Xs compared to 2s may be attributed to the steric bulkiness in the fjord region of Xs-ZP (C40–C2–C1–C15 is −4.4°, C2–C1–C15–C17 is 33.0° based on OM2/MRCI level), which is less than that of 2s-P (C40–C2–C1–C15 is 12.9° and C2–C1–C15–C17 is 39.3° based on OM2/MRCI level). This difference in steric hindrance implies that the rotation from Xs-ZP to the CIs will take more time than for 2s, even though the "dark state" duration is significantly reduced for Xs-ZP compared to 1s-P.

4. Conclusions

In this study, we have introduced a novel molecular motor featuring unidirectional rotational motion through theoretical design. The comprehensive exploration began with the determination of all geometries encompassing conformational changes and the CI point during the photoisomerization rotation of molecular motors, namely 1s, 2s, 6s, and Xs, utilizing both OM2/MRCI and DFT calculations. The optimization of

transition state geometries involved various theoretical methods, revealing the occurrence of two THI barriers during anticlockwise rotation. Significantly, the newly designed molecular motor Xs was identified to possess an exceptionally lower THI barrier compared to 1s, 2s, and 6s, suggesting a substantial acceleration in its rotational speed compared to the aforementioned motors. The study further delved into the Uv-vis absorption spectrum and frontier orbitals. The results indicated a noteworthy red-shift in the maximum absorption wavelength of the newly designed molecular motor Xs. Additionally, a conspicuous reduction in the HOMO–LUMO gap was observed, contributing to the overall red-shift of the Uv-vis absorption spectrum.

TSH simulations at the OM2/MRCI level were employed to investigate the photoisomerization process of 1s, 2s, 6s, and Xs. Remarkably, it was observed that the average lifetime of EP → ZM for Xs is shorter than that of 1s, 2s, and 6s molecular motors. Similarly, ZP → EM is shorter than for 1s and 6s but slightly longer than 2s, with no significant impairment in the quantum yield of the newly designed molecular motor. Calculated time-dependent fluorescence emission spectrum results demonstrated that the "dark state" duration of 1s, 2s, and 6s is significantly longer than that of Xs-EP and Xs-ZP.

In summary, the computational results indicate that the newly proposed light-driven molecular rotary motor Xs exhibits a low thermal helix potential barrier and a simultaneous red-shift in visible light absorption wavelength. In comparison to DDPYM, improvements have been observed in both the UV-visible absorption spectrum and the THI barrier. This work is anticipated to stimulate further research into the design and synthesis of new families of molecular rotary motors.

Conflicts of interest

There are no conflicts to declare.

Acknowledgements

References

1 M. Baroncini, S. Silvi and A. Credi, Photo- and Redox-Driven Artificial Molecular Motors, *Chem. Rev.*, 2020, **120**, 200–268.

2 H. Wang, H. K. Bisoyi, X. Zhang, F. Hassan and Q. Li, Visible Light-Driven Molecular Switches and Motors: Recent Developments and Applications, *Chem. – Eur. J.*, 2022, **28**, e202103906.

15678 | *Phys. Chem. Chem. Phys.*, 2024, **26**, 15672–15680

This journal is © the Owner Societies 2024

3   D. R. S. Pooler, A. S. Lubbe, S. Crespi and B. L. Feringa, Designing light-driven rotary molecular motors, *Chem. Sci.*, 2021, **12**, 14964–14986.

4   N. Koumura, R. W. J. Zijlstra, R. A. van Delden, N. Harada and B. L. Feringa, Light-driven monodirectional molecular rotor, *Nature*, 1999, **401**, 152–155.

5   N. Koumura, E. M. Geertsema, M. B. van Gelder, A. Meetsma and B. L. Feringa, Second Generation Light-Driven Molecular Motors. Unidirectional Rotation Controlled by a Single Stereogenic Center with Near-Perfect Photoequilibria and Acceleration of the Speed of Rotation by Structural Modification, *J. Am. Chem. Soc.*, 2002, **124**, 5037–5051.

6   M. Guentner, M. Schildhauer, S. Thumser, P. Mayer, D. Stephenson, P. J. Mayer and H. Dube, Sunlight-powered kHz rotation of a hemithioindigo-based molecular motor, *Nat. Commun.*, 2015, **6**, 8406.

7   R. Wilcken, M. Schildhauer, F. Rott, L. A. Huber, M. Guentner, S. Thumser, K. Hoffmann, S. Oesterling, R. de Vivie-Riedle, E. Riedle and H. Dube, Complete Mechanism of Hemithioindigo Motor Rotation, *J. Am. Chem. Soc.*, 2018, **140**, 5311–5318.

8   D. I. Pattison and M. J. Davies, *Cancer: Cell Structures, Carcinogens and Genomic Instability*, Birkhäuser Basel, Basel, 2006, pp. 131–157.

9   R. A. van Delden, N. Koumura, A. Schoevaars, A. Meetsma and B. L. Feringa, A donor–acceptor substituted molecular motor: unidirectional rotation driven by visible light, *Org. Biomol. Chem.*, 2003, **1**, 33–35.

10 T. van Leeuwen, J. Pol, D. Roke, S. J. Wezenberg and B. L. Feringa, Visible-Light Excitation of a Molecular Motor with an Extended Aromatic Core, *Org. Lett.*, 2017, **19**, 1402–1405.

11 L. Pfeifer, M. Scherübl, M. Fellert, W. Danowski, J. Cheng, J. Pol and B. L. Feringa, Photoefficient 2nd generation molecular motors responsive to visible light, *Chem. Sci.*, 2019, **10**, 8768–8773.

12 D. Roke, M. Sen, W. Danowski, S. J. Wezenberg and B. L. Feringa, Visible-Light-Driven Tunable Molecular Motors Based on Oxindole, *J. Am. Chem. Soc.*, 2019, **141**, 7622–7627.

13 D. R. S. Pooler, D. Doellerer, S. Crespi and B. L. Feringa, Controlling rotary motion of molecular motors based on oxindole, *Org. Chem. Front.*, 2022, **9**, 2084–2092.

14 L. Greb and J.-M. Lehn, Light-Driven Molecular Motors: Imines as Four-Step or Two-Step Unidirectional Rotors, *J. Am. Chem. Soc.*, 2014, **136**, 13114–13117.

15 D. Roke, S. J. Wezenberg and B. L. Feringa, Molecular rotary motors: Unidirectional motion around double bonds, *Proc. Natl. Acad. Sci. U. S. A.*, 2018, **115**, 9423–9431.

16 L. Greb, A. Eichhöfer and J.-M. Lehn, Synthetic Molecular Motors: Thermal N Inversion and Directional Photoinduced C–N Bond Rotation of Camphorquinone Imines, *Angew. Chem., Int. Ed.*, 2015, **54**, 14345–14348.

17 M. Filatov, M. Paolino, S. K. Min and K. S. Kim, Fulgides as Light-Driven Molecular Rotary Motors: Computational Design of a Prototype Compound, *J. Phys. Chem. Lett.*, 2018, **9**, 4995–5001.

18 J. C. Tully, Molecular dynamics with electronic transitions, *J. Chem. Phys.*, 1990, **93**, 1061–1071.

19 T. Taketsugu, A. Tajima, K. Ishii and T. Hirano, Ab Initio Direct Trajectory Simulation with Nonadiabatic Transitions of the Dissociative Recombination Reaction HCNH+ + e− → HNC/HCN + H, *Astrophys. J.*, 2004, **608**, 323.

20 Y. Ootani, K. Satoh, A. Nakayama, T. Noro and T. Taketsugu, Ab initio molecular dynamics simulation of photoisomerization in azobenzene in the nπ* state, *J. Chem. Phys.*, 2009, **131**, 194306.

21 M. Filatov, M. Paolino, S. K. Min and C. H. Choi, Design and photoisomerization dynamics of a new family of synthetic 2-stroke light driven molecular rotary motors, *Chem. Commun.*, 2019, **55**, 5247–5250.

22 C. García-Iriepa, M. Marazzi, F. Zapata, A. Valentini, D. Sampedro and L. M. Frutos, Chiral Hydrogen Bond Environment Providing Unidirectional Rotation in Photoactive Molecular Motors, *J. Phys. Chem. Lett.*, 2013, **4**, 1389–1396.

23 J. Ma, S. Yang, D. Zhao, C. Jiang, H. Lan and F. Li, Design and Nonadiabatic Photoisomerization Dynamics Study of a Three-Stroke Light-Driven Molecular Rotary Motor, *Int. J. Mol. Sci.*, 2022, **23**, 3908.

24 J. Ma, D. Zhao, L. Yu, C. Jiang, Z. Lan and F. Li, Simultaneously improving the efficiencies of photo- and thermal isomerization of an oxindole-based light-driven molecular rotary motor by a structural redesign, *Phys. Chem. Chem. Phys.*, 2023, **25**, 12800–12809.

25 M. J. Frisch, G. W. Trucks, H. B. Schlegel, G. E. Scuseria, M. A. Robb, J. R. Cheeseman, G. Scalmani, V. Barone, G. A. Petersson, H. Nakatsuji, X. Li, M. Caricato, A. V. Marenich, J. Bloino, B. G. Janesko, R. Gomperts, B. Mennucci, H. P. Hratchian, J. V. Ortiz, A. F. Izmaylov, J. L. Sonnenberg, D. Williams-Young, F. Ding, F. Lipparini, F. Egidi, J. Goings, B. Peng, A. Petrone, T. Henderson, D. Ranasinghe, V. G. Zakrzewski, J. Gao, N. Rega, G. Zheng, W. Liang, M. Hada, M. Ehara, K. Toyota, R. Fukuda, J. Hasegawa, M. Ishida, T. Nakajima, Y. Honda, O. Kitao, H. Nakai, T. Vreven, K. Throssell, J. A. Montgomery Jr., J. E. Peralta, F. Ogliaro, M. J. Bearpark, J. J. Heyd, E. N. Brothers, K. N. Kudin, V. N. Staroverov, T. A. Keith, R. Kobayashi, J. Normand, K. Raghavachari, A. P. Rendell, J. C. Burant, S. S. Iyengar, J. Tomasi, M. Cossi, J. M. Millam, M. Klene, C. Adamo, R. Cammi, J. W. Ochterski, R. L. Martin, K. Morokuma, O. Farkas, J. B. Foresman and D. J. Fox, *Gaussian 09, Revision D.01*, Gaussian, Inc., Wallingford CT, 2013.

26 X. Zhuang, J. Wang and Z. Lan, Photoinduced Nonadiabatic Decay and Dissociation Dynamics of Dimethylnitramine, *J. Phys. Chem. A*, 2013, **117**, 4785–4793.

27 X. Pang, X. Cui, D. Hu, C. Jiang, D. Zhao, Z. Lan and F. Li, Watching the Dark State in Ultrafast Nonadiabatic Photoisomerization Process of a Light-Driven Molecular Rotary Motor, *J. Phys. Chem. A*, 2017, **121**, 1240–1249.

28 A. Nikiforov, J. A. Gamez, W. Thiel and M. Filatov, Computational Design of a Family of Light-Driven Rotary Molecular

This journal is © the Owner Societies 2024

Phys. Chem. Chem. Phys., 2024, **26**, 15672–15680 | 15679

Motors with Improved Quantum Efficiency, *J. Phys. Chem. Lett.*, 2016, **7**, 105–110.

29 M. Che, Y.-J. Gao, Y. Zhang, S.-H. Xia and G. Cui, Electronic structure calculations and nonadiabatic dynamics simulations of excited-state relaxation of Pigment Yellow 101, *Phys. Chem. Chem. Phys.*, 2018, **20**, 6524–6532.

30 Y.-H. Zhang, X.-W. Sun, T.-S. Zhang, X.-Y. Liu and G. Cui, Nonadiabatic Dynamics Simulations on Early-Time Photochemistry of Spirobenzopyran, *J. Phys. Chem. A*, 2020, **124**, 2547–2559.

31 Y.-J. Gao, X.-P. Chang, X.-Y. Liu, Q.-S. Li, G. Cui and W. Thiel, Excited-State Decay Paths in Tetraphenylethene Derivatives, *J. Phys. Chem. A*, 2017, **121**, 2572–2579.

32 S.-H. Xia, M. Che, Y. Liu, Y. Zhang and G. Cui, Photochemical mechanism of 1,5-benzodiazepin-2-one: electronic structure calculations and nonadiabatic surface-hopping dynamics simulations, *Phys. Chem. Chem. Phys.*, 2019, **21**, 10086–10094.

33 O. Weingart, Z. Lan, A. Koslowski and W. Thiel, Chiral Pathways and Periodic Decay in *cis*-Azobenzene Photodynamics, *J. Phys. Chem. Lett.*, 2011, **2**, 1506–1509.

34 Z. Lan, Y. Lu, O. Weingart and W. Thiel, Nonadiabatic Decay Dynamics of a Benzylidene Malononitrile, *J. Phys. Chem. A*, 2012, **116**, 1510–1518.

35 Y.-T. Wang, X.-Y. Liu, G. Cui, W.-H. Fang and W. Thiel, Photoisomerization of Arylazopyrazole Photoswitches: Stereospecific Excited-State Relaxation, *Angew. Chem., Int. Ed.*, 2016, **55**, 14009–14013.

36 X. Pang, C. Jiang, Y. Qi, L. Yuan, D. Hu, X. Zhang, D. Zhao, D. Wang, Z. Lan and F. Li, Ultrafast unidirectional chiral rotation in the Z–E photoisomerization of two azoheteroarene photoswitches, *Phys. Chem. Chem. Phys.*, 2018, **20**, 25910–25917.

37 G. Cui, Z. Lan and W. Thiel, Intramolecular Hydrogen Bonding Plays a Crucial Role in the Photophysics and Photochemistry of the GFP Chromophore, *J. Am. Chem. Soc.*, 2012, **134**, 1662–1672.

38 N. Otte, M. Scholten and W. Thiel, Looking at Self-Consistent-Charge Density Functional Tight Binding from a Semiempirical Perspective, *J. Phys. Chem. A*, 2007, **111**, 5751–5755.

39 M. R. Silva-Junior and W. Thiel, Benchmark of Electronically Excited States for Semiempirical Methods: MNDO, AM1, PM3, OM1, OM2, OM3, INDO/S, and INDO/S2, *J. Chem. Theory Comput.*, 2010, **6**, 1546–1564.

40 W. Thiel, Semiempirical quantum–chemical methods, *Wiley Interdiscip. Rev.: Comput. Mol. Sci.*, 2014, **4**, 145–157.

41 T. W. Keal, M. Wanko and W. Thiel, Assessment of semiempirical methods for the photoisomerisation of a protonated Schiff base, *Theor. Chem. Acc.*, 2009, **123**, 145–156.

42 W. Weber and W. Thiel, Orthogonalization corrections for semiempirical methods, *Theor. Chem. Acc.*, 2000, **103**, 495–506.

43 W. Thiel, *MNDO Program, Version7.0*, Max-Planck-Institut fur Kohlenforschung, Mulheim, Germany, 2007.

44 T. W. Keal, A. Koslowski and W. Thiel, Comparison of algorithms for conical intersection optimisation using semiempirical methods, *Theor. Chem. Acc.*, 2007, **118**, 837–844.

45 L. Du and Z. Lan, An On-the-Fly Surface-Hopping Program JADE for Nonadiabatic Molecular Dynamics of Polyatomic Systems: Implementation and Applications, *J. Chem. Theory Comput.*, 2015, **11**, 1360–1374.

46 A. Prlj, D. Hollas and B. F. E. Curchod, Deciphering the Influence of Ground-State Distributions on the Calculation of Photolysis Observables, *J. Phys. Chem. A*, 2023, **127**, 7400–7409.

47 G. Granucci, M. Persico and A. Zoccante, Including quantum decoherence in surface hopping, *J. Chem. Phys.*, 2010, **133**, 134111.

48 W. C. Swope, H. C. Andersen, P. H. Berens and K. R. Wilson, A computer simulation method for the calculation of equilibrium constants for the formation of physical clusters of molecules: Application to small water clusters, *J. Chem. Phys.*, 1982, **76**, 637–649.

49 A. V. Karnik and M. Hasan, in *Stereochemistry*, ed. A. V. Karnik and M. Hasan, Elsevier, 2021, pp. 49–91.

50 J. Ma, D. Zhao, C. Jiang, Z. Lan and F. Li, Effect of Temperature on Photoisomerization Dynamics of a Newly Designed Two-Stroke Light-Driven Molecular Rotary Motor, *Int. J. Mol. Sci.*, 2022, **23**, 9694.

51 A. Kazaryan, Z. Lan, L. V. Schäfer, W. Thiel and M. Filatov, Surface Hopping Excited-State Dynamics Study of the Photoisomerization of a Light-Driven Fluorene Molecular Rotary Motor, *J. Chem. Theory Comput.*, 2011, **7**, 2189–2199.

15680 | *Phys. Chem. Chem. Phys.*, 2024, **26**, 15672–15680

This journal is © the Owner Societies 2024